RESEARCH PAPER

Capillary-driven pumping for passive degassing and fuel supply in direct methanol fuel cells

Nils Paust · Christian Litterst · Tobias Metz · Michael Eck · Christoph Ziegler · Roland Zengerle · Peter Koltay

Abstract In this paper we present a new concept of creating and using capillary pressure gradients for passive degassing and passive methanol supply in direct methanol fuel cells (DMFCs). An anode flow field consisting of parallel tapered channels structures is applied to achieve the passive supply mechanism. The flow is propelled by the surface forces of deformed CO_2 bubbles, generated as a reaction product during DMFC operation. This work focuses on studying the influence of channel geometry and surface properties on the capillary-induced liquid flow rates at various bubbly gas flow rates. Besides the aspect ratios and opening angles of the tapered channels, the static contact angle as well as the effect of contact angle hysteresis has been identified to significantly influence the liquid flow rates induced by capillary forces at the bubble menisci. Applying the novel concept, we show that the liquid flow rates are up to thirteen times higher than the methanol oxidation reaction on the anode requires. Experimental results are presented that demonstrate the continuous passive operation of a DMFC for more than 15 h.

List of symbols

A_{MEA}	Chemical active area of the DMFC (cm^2)
C_f	Concentration of the aqueous methanol water solution (m l^{-1})

N. Paust (✉) · C. Litterst · T. Metz · M. Eck · C. Ziegler · R. Zengerle · P. Koltay
Laboratory for MEMS Applications,
Department of Microsystems Engineering (IMTEK),
University of Freiburg, Georges-Koehler-Allee 106,
79110 Freiburg, Germany
e-mail: nils.paust@imtek.de

F	Faraday constant ($F = 96485°C$ mol^{-1})
g	Ground acceleration (9.81 m s^{-1})
h	Channel height at the channel inlet (mm)
H	Channel height at the inlet of the double tapered structure (mm)
I	Electric current (mA)
i	Electric current density (mA cm^{-2})
l	Length of the channel (mm)
L_{bub}	Length of a gas bubble (mm)
$\dot{m}$	Mass flow (kg s^{-1})
M_{CO_2}	Molar weight of CO_2 ($M_{CO_2} = 44$ g mol^{-1})
M_{CH_3OH}	Molar weight of CH_3OH ($M_{CH_3OH} = 32$ g mol^{-1})
p	Pressure (Pa)
Δp_{bub}	Pressure difference over a deformed gas bubble in a tapered channel (Pa)
p_{eff}	Pump efficiency defined as the ratio between the liquid flow rate induced by the moving bubbles to the bubbly gas flow rate (−)
P	Electric power (mW)
r	Radius of a liquid gas interface (mm)
V	Volume of the reservoir filling (ml)
w	Channel width (mm)
W	Channel width of the centre channel of the double-tapered channel (mm)
x	Horizontal coordinate
x_f	x position of bubble front meniscus (mm)
x_b	x position of bubble back meniscus (mm)
y	Vertical coordinate
α	Opening angle of the tapered channel (°)
β	Opening angle of the side channels of the double-tapered channel (°)
θ	Contact angle (°)
θ_{hys}	Contact angle hysteresis (°)
θ_{ad}	Advancing contact angle (°)

θ_{rec}	Receding contact angle (°)
θ_{pin}^{inlet}	Contact angle caused by pinning at the gas inlet (°)
Φ	Flow rate (μl min^{-1})
κ	Curvature of the liquid/gas interface (mm^{-1})
ρ	Density (at ambient conditions: methanol solution 4 M: $\rho_l = 968$ kg m^{-3}; gas: $\rho_{CO_2} = 1.78$ kg m^{-3})
σ	Surface tension (methanol solution 4 M: 0.053 N m^{-1})

1 Introduction

Portable direct methanol fuel cells (DMFCs) are very attractive due to the high energy density of methanol, quick refueling and potentially unlimited shelf life (Dyer 2002). Therefore, they are promising candidates for powering small electronic devices. Despite this potential, the DMFC still faces significant drawbacks. In addition to methanol crossover (Jian and Chu 2004), a low catalytic activity of the methanol reaction because of CO poisoning (Park et al. 2004) and flooding of the cathode (Lu and Wang 2004), the efficient removal of carbon dioxide bubbles from the anode is critical (Yang and Zhao 2005) and has thus been studied experimentally (Wong et al. 2005; Yang et al. 2005a, b) as well as theoretically (Fei et al. 2008).

At the anode, CO_2 bubbles are generated as a reaction product of the methanol oxidation reaction (MOR) and may block channels, hinder fuel supply and cause the DMFC to malfunction. With respect to small portable appliances, the common approach to deliver methanol and flush out CO_2 bubbles by an ancillary liquid pump is very inefficient because it consumes a significant amount of energy and makes the system large and complex reducing the overall energy density. Therefore, the recently proposed so-called passive DMFC is promising, as it operates fully autonomously without any external pumps and valves (Liu et al. 2005; Kho et al. 2005; Chan et al. 2007). However, the majority of these passive DMFCs supply methanol by diffusion or gravitational effects and the removal of CO_2 is achieved by the buoyancy of the bubbles. Thus, the fuel cell is limited in its orientation and the methanol reservoir must be directly attached to the fuel cell in order to reduce the diffusion length. To account for this challenge, bubble actuated pumping principles as presented by e.g. Ateya et al. (2004), Cheng et al. (2007) and Meng and Kim (2008) are attractive because these concepts potentially can combine degassing of CO_2 and methanol supply without the need of any external components when applied to a DMFC. The most relevant approach with respect to the current work is presented by Meng and Kim (2008) describing a pumping mechanism based on directional growth and venting of bubbles. A gas-blocking

element on one side and a degassing plate on the other side of a microchannel cause the bubbles to grow towards the degassing plate where the bubbles are vented. The growing bubbles push liquid out of the channel and bubbles vented through the degassing plate suck liquid into the system. For the control of liquid flow rates, all existing methods use externally controlled parameters such as the applied electrical voltage or frequency for the electrochemically actuated micropumps (e.g. Ateya et al. 2004; Cheng et al. 2007; Meng and Kim 2008). However, for the passive DMFCs it is also of interest to be able to adjust the liquid flow rates by design, even if the rate of the electrochemical conversion and thus the gas flow rate is fixed. In contrast to previous work, the present work applies tapered channel structures for capillary-force-driven bubble transport. The moving bubbles displace liquid at the front and suck liquid into the system at the back side, so passive fuel circulation inside a DMFC can be realized. The following experimental study shows that the presented mechanism allows for the variation of the liquid flow rates induced by moving bubbles from 0.5 up to 13% of the volumetric gas flow rate by changing the design parameters of the flow field. Thus, the amount of liquid transported by the bubbles can be adjusted to the needs of a specific DMFC even at a fixed rate of the electrochemical conversion.

The proposed pumping mechanism is propelled by the surface forces of intrinsically generated and deformed CO_2 bubbles. In our previous work (Litterst et al. 2006) we have shown that an appropriate channel design can transport CO_2 gas bubbles to an outlet in a passive manner. No external pressure gradient is needed to transport CO_2 gas, and clogging of gas bubbles that may hinder fuel supply is prevented. In the present work, the moving bubbles additionally pump the fuel in order to achieve fully autonomous operation. The application of passive degassing and fuel supply in DMFCs was first proposed by Paust et al. (2008). In the following, a comprehensive study on the influence of channel configuration is presented. In particular, the impact of the overall shape of the channel, the opening angle α of the tapered channels, and the wetting properties of the channel walls, on the passive pumping mechanism is investigated.

2 Capillary pumping mechanism

2.1 Working principle

In a tapered channel with hydrophilic channel walls ($\theta \ll 90°$) of which a side view is schematically depicted in Fig. 1a, a growing bubble that touches the upper and lower channel wall becomes deformed. The tapering causes a continuous increase of the channel cross-section in

Fig. 1 **a** Schematic side view of a growing bubble deformed by the top and bottom surface in a tapered channel with opening angle α. t_1 Bubble starts to grow into the channel, t_2 Bubble touches upper channel wall, t_3 Bubble grows towards the outlet, but contact-line pinning keeps the bubble from moving, t_4 Contact-line pinning has reached a maximum value. The deformed bubble detaches from the inlet and moves towards the increasing cross-section of the channel. **b** Schematic top view of moving bubbles in a tapered channel. **b**(*i*) blocking mode **b**(*ii*) non-blocking mode. **c** Channel geometries for capillary-driven degassing and liquid pumping in passive DMFCs. **c**(*i*) Single-tapered channel **c**(*ii*) double-tapered T-shaped channel. **d** Cross-sections of possible bubble shapes (*white*) in T-shaped channels
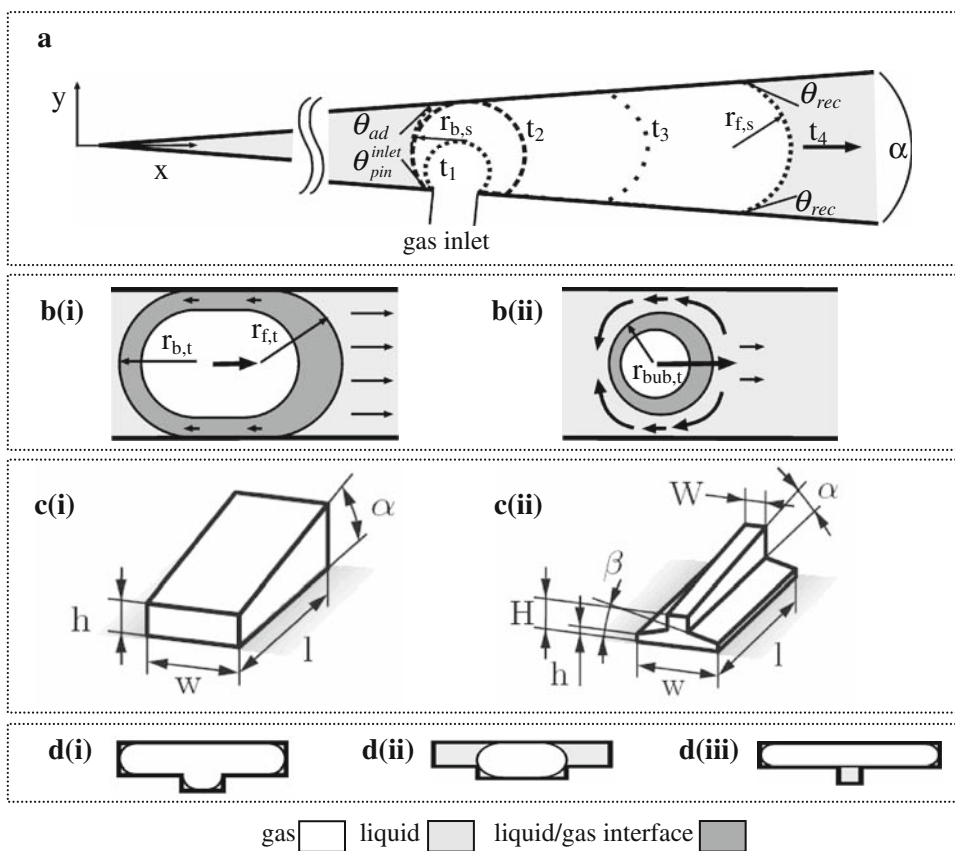
x-direction, thus, the deformed bubbles exhibits interfaces with different curvatures at the front and the back of the bubble which leads to a pressure difference over the whole bubble, according to the law of Young–Laplace.

This capillary pressure difference induces a liquid flow from the front to the back of the bubble, transporting the bubble towards the larger channel cross-section. However, before a bubble starts moving, the three-phase contact lines typically pin at the channel walls, leading to a contact angle hysteresis (Fig. 1a, $t = t_3$): $\theta_{hys} = \theta_{ad} - \theta_{rec}$. The hysteresis is a result of surface roughness and chemical heterogeneities at the solid–liquid–gas interface (Gao and McCarthy 2006) and leads to a so-called pinning force resisting the bubble movement. The growing bubble remains fixed until the contact angle hysteresis reaches a maximum value. Further growth causes the bubble to detach from its origin and to move towards the increasing channel cross-section (Fig. 1a, $t = t_4$). Depending on the size of the detaching bubbles, two different pumping modes can be realized, a blocking and a non-blocking pumping mode. As schematically depicted in Fig. 1b, showing top views of moving bubbles in tapered channels, a moving bubble blocking the channel transports the major fraction of the displaced liquid out of the channel which means that liquid is effectively pumped. A minor fraction

flows to the back of the bubble due to corner flow along the channel edges. In the non-blocking mode [Fig. 1b(ii)], a comparatively large liquid bypass remains so that the major fraction of the displaced liquid flows directly around the bubble, thus not contributing to the pumping mechanism.

2.2 Channel configurations and pumping modes

The investigated channel designs for passive bubble-driven fluid transport are depicted in Fig. 1c and the geometric parameters are listed in Table 1.

In the single-tapered channel as depicted in Fig. 1c(i), the different pumping modes can be realized by changing wetting properties, opening angles and aspect ratios as discussed later. In T-shaped channels, as depicted in Fig. 1c(ii), depending on geometric parameters, gas bubbles can block the T-channel [Fig. 1d(i)], fill the root [Fig. 1d(ii)], or fill the branch of the T [Fig. 1d(iii)] only. Unlike rectangular channels, the configuration Fig. 1d(ii) and d(iii) ensures the non-blocking pumping mode and increases bubble mobility due to unblocked liquid bypasses, even if large bubbles occur. A discussion on the parameter range leading to the different bubble configurations of Fig. 1d is presented in Litterst et al. (2008). In the current paper, the geometric parameters listed in Table 1

Table 1 Geometric data of the investigated channels

	w (mm)	W (mm)	h (mm)	H (mm)	l (mm)	β (°)
Single-tapered; $\alpha = 1.5°$	3	–	0.8	–	20	–
Single-tapered; $\alpha = 3°$	3	–	0.8	–	20	–
T-shaped double-tapered; $\alpha = 1.5°$	3	0.8	0.3	0.8	20	10
T-shaped double-tapered; $\alpha = 3°$	3	0.8	0.3	0.8	20	10

have been chosen to always ensure configuration Fig. 1d(ii).

2.3 Modeling

In the following, a model for the estimation of pumping modes in single-tapered channels is presented. It is developed for a stationary growing bubble without any external forces acting on it. During the operation of the bubble pump however, the complex interaction of the growth and movement of several bubbles in parallel may cause a deviation from the estimated pumping modes. Nevertheless, using the model one can understand the influence of the different parameters such as opening angle and wetting properties on the pumping mechanism and estimate pumping modes occurring in the channels. Thus, the model is an appropriate tool for an initial design of a tapered channel flow field for passive DMFC operation.

As mentioned above, growing bubbles in a tapered channel become deformed by the channel walls, causing a pressure difference over the whole bubble. According to the law of Young–Laplace this pressure difference is a function of the surface tension σ and the curvatures κ_f and κ_b of the liquid–gas interfaces at the front and the back of the bubble, respectively:

$$\Delta p_{\text{bub}} = 2\sigma(\kappa_b - \kappa_f) \tag{1}$$

The curvatures κ_b and κ_f of the interfaces at both bubble ends can be calculated at any reference point by its tangential plane and the two main radii. The main radii arise in planes which are perpendicular to the tangential plane of the interface and perpendicular to each other (Langbein 2002). Two of such planes are projections of the bubble from the top and the side of the channel. The curvatures can thus be calculated as:

$$\begin{aligned}\kappa_b &= \frac{1}{2}\left(\frac{1}{r_{b,t}} + \frac{1}{r_{b,s}}\right) \\ \kappa_f &= \frac{1}{2}\left(\frac{1}{r_{f,t}} + \frac{1}{r_{f,s}}\right)\end{aligned} \tag{2}$$

The subscript of the radii t and s stand for top view and side view of the bubble. Assuming there is no external pressure gradient applied, just before the bubble starts moving, there is no pressure difference over the bubble ($\Delta p_{\text{bub}} = 0$) with equal curvatures of the interfaces at the

front and the back of the bubble and the contact angle hysteresis of the three-phase contact line reaches a maximum value. As long as the bubble does not touch the side walls, it is assumed that the top projection of the bubble forms a perfect circle with $r_{f,t} = r_{b,t} = r_{\text{bub},t}$ and the curvatures of the bubble therefore yield:

$$\begin{aligned}\kappa_b &= \frac{1}{2}\left(\frac{1}{r_{\text{bub},t}} + \frac{\frac{1}{2}\left[\cos\left(\theta_{ad}+\frac{\alpha}{2}\right)+\cos\left(\theta_{\text{pin}}^{\text{inlet}}+\frac{\alpha}{2}\right)\right]}{y_b}\right) \\ \kappa_f &= \frac{1}{2}\left(\frac{1}{r_{\text{bub},t}} + \frac{\cos\left(\theta_{rec}-\frac{\alpha}{2}\right)}{y_f}\right)\end{aligned} \tag{3}$$

where θ_{ad} and θ_{rec} are the advancing and the receding contact angle, respectively, $\theta_{\text{pin}}^{\text{inlet}}$ is the contact angle caused by contact line pinning at the gas inlet, α is the opening angle of the tapered channel and y_f and y_b are the half channel heights at the front and the back meniscus position, respectively. Inserting Eq. 3 in Eq. 1, the bubble radius of the top projection $r_{\text{bub},t}$ vanishes. Because of contact angle hysteresis, the contact angles of an advancing and receding interface are unequal. In the present paper, the standard convention is used that is also applied for the study of advancing and receding liquid interfaces (Gao and McCarthy 2006). Therefore, the contact angle at the rear of the bubble is named "advancing" and the one at the bubble front is the "receding" contact angle. Due to the gas inlet forming an additional obstacle for the moving contact line, the advancing contact angle has to be divided into the one at the "flat" wall and the one pinning at the gas inlet. If the bubble size grows larger than the channel width, the bubble blocks the complete channel and becomes additionally deformed by the side walls. The radii of the interfaces must then be calculated by:

$$\begin{aligned}\kappa_b &= \frac{1}{2}\left(\frac{\frac{1}{2}\left[\cos\left(\theta_{ad}+\frac{\alpha}{2}\right)+\cos\left(\theta_{\text{pin}}^{\text{inlet}}+\frac{\alpha}{2}\right)\right]}{y_b} + \cos\left(\theta_{ad}^{\text{side}}\right)\frac{2}{w}\right) \\ \kappa_f &= \frac{1}{2}\left(\cos\left(\theta_{rec}-\frac{\alpha}{2}\right)\frac{1}{y_f} + \cos\left(\theta_{rec}^{\text{side}}\right)\frac{2}{w}\right)\end{aligned} \tag{4}$$

where w is the channel width. Due to possibly different wetting properties of the channel side walls compared to the channel bottom, again the contact angles at the side walls $\theta_{ad}^{\text{side}}$ and $\theta_{rec}^{\text{side}}$ must be treated independently. For the calculation of pumping modes, it is sufficient to calculate the bubble length in x direction because of the assumption of the top projection forming a circle as long as the bubble

does not touch the side walls. If the bubble length exceeds the channel width the bubble length in y direction yields the channel width w. The bubble length in x direction L_{bub} can be determined by:

$$L_{bub} = x_f - x_b$$
$$+ r_b \left(2 - \sin\left(\pi - \theta_{pin}^{inlet} + \frac{\alpha}{2} \right) - \sin\left(\pi - \theta_{rec} - \frac{\alpha}{2} \right) \right).$$
$$(5)$$

Here, x_b is the minimum x value of the triple line at the channel wall. In the experimental configuration, x_b is the x coordinate of the gas inlet. x_f is the maximum x value of the triple line at the wall. At the pinning threshold, with $y = x\tan(\alpha/2)$, x_f can be derived from Eqs. 1 and 3 to yield $L_{bub} < w$ in the non-blocking mode and from Eqs. 1 and 4 to yield $L_{bub} > w$ in the blocking mode. With these equations, the pumping modes in dependency on the geometric parameters and the contact angles at the walls can be calculated for the single-tapered channel.

2.4 A note on gravity

The current work analyses the liquid flow induced by capillary actuated bubbles. In order to account for possible errors caused by gravitational effects, a brief discussion on the influence of gravity is performed in the following. The bond number describes the ratio of gravitational to capillary surface forces (Nguyen and Wereley 2002):

$$Bo = \frac{(\rho_l - \rho_g)L^2 g}{\sigma} \qquad (10)$$

In the considered setting, the characteristic length L is given by the diameter of a gas bubble. The volume of the largest bubble was roughly estimated to be 14 µl. The Bond number for a bubble of that size is $Bo = 1.6$, indicating that gravity cannot be neglected. To account for this fact, the experimental set-up was designed so that there is no difference in hydrostatic height during the movement of bubbles inside the channels. At the channel outlet and in the reservoir where the bubbles rise due to buoyancy, there is a large bypass for the liquid to keep the influence of gravity on the induced flow rates comparatively small.

2.5 The passive DMFC

Figure 2a shows a schematic of the set-up of the considered fully passive DMFC with the incorporated bubble-driven fuel circulation mechanism.

The anode flow field consists of three parallel tapered channels as depicted in Fig. 1c that open up towards a reservoir. Carbon dioxide is generated at the catalyst layer on the anode of the membrane electrode assembly (MEA) forming gas bubbles. These gas bubbles are transported out of the channel into the reservoir by the capillary transport mechanism described in Sect. 2.1. Thereby, the bubbles push liquid out of the channel at the front and drag liquid in

Fig. 2 a Schematic, **b** exploded view and **c** photograph of the fully passive DMFC with the following components: *1* reservoir, *2* anode flow field, *3* electrical contacts, *4* PDMS sealing, *5* porous transport layer, *6* membrane electrode assembly, *7* cathode flow field, *8* lower mounting plate
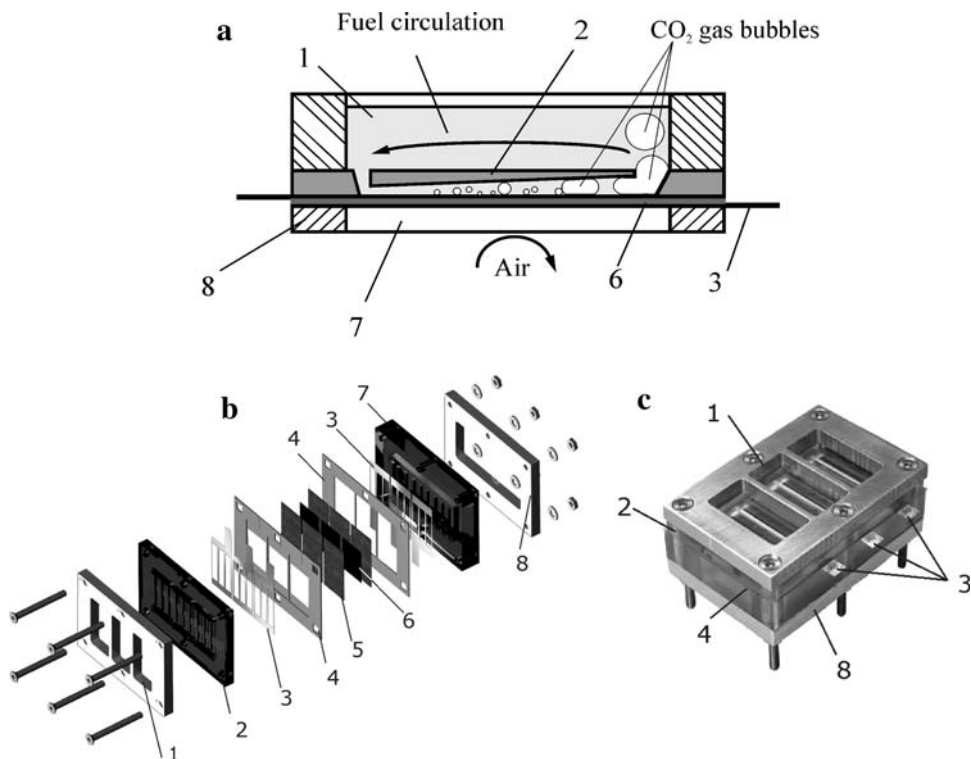
the channel at the back. As a result, a passive fuel circulation through the channels and the reservoir is induced that continuously transports methanol to the reactive area of the MEA. This passive fuel circulation is quantified in terms of the pump efficiency p_{eff}, defined as the ratio of the volumetric liquid flow rate induced by the moving CO_2 bubbles to the volumetric gas flow rate. In the following, the required pump efficiency to deliver the amount of methanol that is consumed by the MOR is derived from the stoichiometry of the MOR at the anode:

$$CH_3OH + H_2O \rightarrow CO_2 + 6H^+ + 6e^- \qquad (6)$$

At a given electric current I of the operating fuel cell, the mass flow of the generated carbon dioxide can be calculated as:

$$\dot{m}_{CO_2} = \frac{I}{6F} M_{CO_2}. \qquad (7)$$

Here, M_{CO_2} is the molar mass of carbon dioxide, and F is the Faraday constant. The mass flow of methanol required to sustain the operation generating the current I consists of two parts, the mass flow consumed by the MOR that produces the electrons, the protons, and the carbon dioxide, and methanol losses mainly caused by methanol crossover:

$$\dot{m}_{CH_3OH} = \dot{m}_{MOR} + \dot{m}_{loss} \qquad (8)$$

The methanol consumption caused by the MOR can be calculated according to the law of Faraday:

$$\dot{m}_{CH_3OH}^{MOR} = \frac{I}{6F} M_{CH_3OH} \qquad (9)$$

For passive operation, it is assumed that the circulating methanol/water solution is saturated with carbon dioxide, so all produced CO_2 is considered to be a bubbly gas flow. Thus, with Eqs. 7 and 9, the minimum pump efficiency for the MOR can be calculated as:

$$p_{eff}^{MOR} = \frac{\rho_{CO_2}}{M_{CO_2} C_f} \qquad (10)$$

with C_f as the methanol concentration in the fuel. Typically, methanol is fed with a molar concentration between 0.5 and 4 mol l^{-1}. In passive fuel cells, a comparatively high methanol concentration is preferred (Liu et al. 2005). The experiments for the present work were made using a four molar methanol solution for which p_{eff}^{MOR} calculates to 1%.

As reported by Jian and Chu 2004, methanol losses caused by crossover depend on the MEA type and thickness, the concentration of methanol at the anode catalyst layer, the operating temperature of the DMFC and on the discharging current. These terms highly depend on the specific components and operating conditions of the DMFC. Since the aim of the present paper is to present a

general approach for passive degassing and fuel supply in DMFCs, the reference value used to evaluate the pumping mechanism is the methanol consumption by the MOR only. However, Jian and Chu 2004 reported that methanol consumption by crossover can exceed the consumption by the MOR by far. Chan et al. (2008) studied crossover in a specific passive DMFC in which the crossover flow was estimated to be 2.7 times higher than the consumption by the MOR. Thus, methanol crossover cannot be neglected. In the present paper, methanol crossover is accounted for by ensuring that the liquid flow rates transported by the bubble-driven actuation principle are several times higher than the methanol consumption rate caused by the MOR.

3 Experimental

3.1 Experimental set-up

In order to obtain defined boundary conditions, in particular a well-defined gas flow, the pumping performance was studied in an experimental set-up as illustrated in Fig. 3. In this experiment, the gas flow is supplied by three syringe pumps connected to individual gas inlets by stiff Teflon® tubes with an inner diameter of 500 μm, a wall thickness of 230 μm and a length of 50 mm. A tapered channel, manufactured by hot embossing into PMMA as described by Becker and Gärtner (2000), is sealed with a PMMA cover with drilled holes of 600 μm in diameter serving as gas inlets. The master moulds for the hot embossing of the single tapered and the double tapered T-shaped channels were fabricated by micro milling performed by FWB GmbH. Reservoirs are attached to the channel outlets and inlets and are clamped together with the channels and the cover by screws. The methanol inlets and outlets are connected via a flow sensor (Sensirion ASL1430-16). The growth and
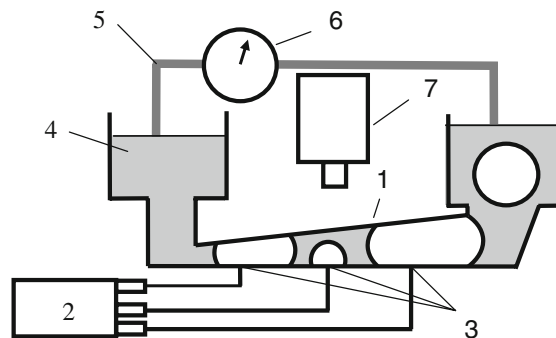
Fig. 3 Experimental set-up for the investigation of pump rates induced by moving gas bubbles in tapered channel structures. *1* tapered channel structure, *2* three syringe pumps, *3* three individual gas inlets, *4* reservoir, *5* tubing, *6* flow sensor, *7* camera

movement of gas bubbles were observed with a camera (μ-eye UI-2230-C). To vary the wetting properties, a hydrophilic configuration was realized by coating the channel walls with a silicate oxide layer by flame pyrolysis using Nanoflame NFo2 from Polytec. The static advancing contact angle on plain PMMA was measured to be $\theta_{ad} = 33°$. A contact angle of $\theta_{ad} = 5° \pm 3°$ was measured on a surface treated with the silicate oxide layer.

For the fuel cell performance measurements, a computer controlled power supply with internal current control (TTi PL330DP) and an analog digital transformer card (Meilhaus ME-4610) to acquire the voltage data were used. The triggering of the current source and the read-out of the measure instruments (ammeter and voltmeter) were controlled via a routine, programmed in Testpoint version 4.1. Galvanostatic measurements were performed for which the electric current was controlled by the power supply and the voltage data was acquired every two-seconds.

3.2 Manufacturing of the passive DMFC

Figure 2b shows an exploded view of the fabricated DMFC system. The device consists of three cells containing different channel configurations. Each anode flow field comprises three parallel channels that end up in a gas collection channel which is connected with the inlet of the channel through the reservoir to enable fuel circulation. The tapered channel flow fields of the DMFC were again fabricated by hot embossing in PMMA. Afterwards, collection channels were fabricated by milling with a taper angle of 10° at both ends of the flow field. The electrical contacts were manufactured by laser cutting of stainless steel (100 µm thickness) and electroplated with a 5 µm gold layer. The sealing consists of vacuum casted PDMS. The 100 µm thick MEA (Umicore) had a catalyst loading of 1.5 mg cm^{-2} on the anode side and 1.8 mg cm^{-2} on the cathode side. The active area of a single cell is $A_{MEA} = 3$ cm^2.

For the cathode, a PMMA end plate with three rectangular wholes for passive diffusive oxygen supply was also manufactured by hot embossing.

4 Results

The experimental work is structured as follows: first, the growth and detachment of bubbles above the three different gas inlets was observed in order to investigate the pumping modes of moving gas bubbles at different opening angles. The data are compared to the model for the calculation of pumping modes. Secondly, the pump efficiency of moving bubbles was studied for different channel types at various gas flow rates. The influence of the pumping modes on the

pumping efficiency and the applicability for passive DMFC supply are discussed. Finally, two channel configurations were used to study the performance of passively operating DMFCs.

4.1 Bubble detachment and pumping modes

The channels were filled with a four molar water methanol solution and air was pumped into the channel at three positions with the syringe pumps at a flow rate of 2.5 µl min^{-1}. With the camera attached to a microscope, the point of bubble detachment was determined. The length of the bubbles at the detachment point was measured and plotted against the distance of the three different gas inlets from the liquid inlet (Fig. 4). It can be seen that in the 1.5° channel all bubbles breaking up from the gas inlets are larger than the channel width plotted by the dash-dotted line, which means that this channel exhibits the blocking mode. In the 3° channel, gas bubbles formed above the first two inlets do not block the channel when they start to move towards the outlet. Only the last inlet shows the blocking mode.

For the theoretical evaluation performed with Eqs. 1–5, all contact angles except the contact angle caused by pinning at the inlet θ_{pin}^{inlet} were determined experimentally. The flame pyrolysis coating turned out to be anisotropic, therefore, as mentioned above, the contact angles at the side walls were treated independently of the contact angles at the top of the channel. The contact angles on the side wall were determined by analyzing photographs of the top views on moving bubbles. The advancing side wall contact angle was measured to be $\theta_{ad}^{side} = 25° \pm 2°$, the receding one was $\theta_{rec}^{side} = 15° \pm 2°$. The advancing contact angles on the top walls were measured by the "sessile drop
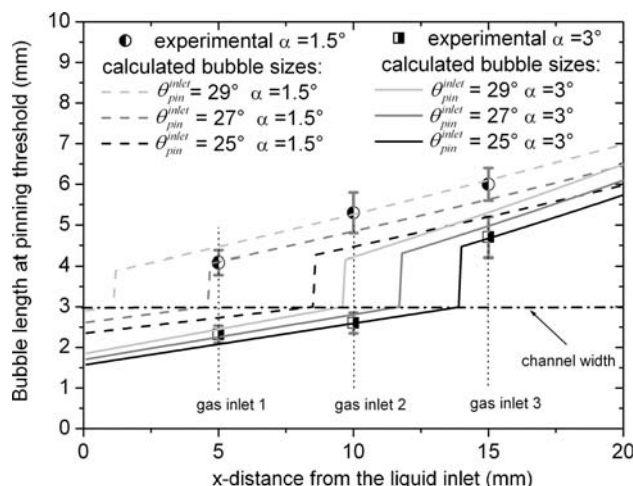
Fig. 4 Experimentally and theoretically determined bubble length of growing bubbles overcoming the pinning threshold plotted against the distance of the bubble back meniscus from the channel inlet

method" on a OCA 15 plus measure set-up manufactured by Dataphysics^{TM} to $\theta_{ad} = 5° \pm 3°$ and $\theta_{rec} = 0°$. With these parameters, the bubble sizes calculated with Eqs. 1, 3 and 5 (non-blocking mode) or Eqs. 1, 4 and 5 (blocking mode) are also plotted in Fig. 4 for three different values of contact line pinning at the gas inlet. The discontinuity of the graphs at $L_{bub} = 3$ mm as the bubble length exceeds the channel width is due to the formation of additional contact-lines at the side walls of the channel. These contact-lines are also subject to contact-line pinning. Therefore, an additional resistance for the moving bubbles arises and the bubbles must grow larger as indicated by the discontinuity so that their capillary pressure overcomes the additional resistance and the bubbles start moving.

As depicted in Fig. 4, a comparison of the calculated curves with the experimental data shows that the contact line pinning at the inlets leads to contact angles situated between $\theta_{ad}^{inlet} = 25°$ and $\theta_{ad}^{inlet} = 29°$.

A bubble sequence showing a growing bubble in a 3°-tapered channel above inlet 2 ($x = 10$ mm) is depicted in Fig. 5. The bubble exhibits the non-blocking mode when it starts to move. The critical reader might argue that the assumptions of a constant curvature along the top view of the interfaces of the bubble does not hold true due to the phenomenon of bubble necking as observed in Fries and Rohr (2008) during the break-up from the inlet nozzle. However, taking a closer look at the bubble growth above an inlet at the gas flow rate considered and without any external actuation, one will see that shortly before the bubble starts moving towards the outlet (Fig. 5c), there is hardly any necking visible.

Another source of error is the interaction of fluid dynamics of the three gas inlets actuated in parallel when analyzing the pump performance of a complete channel. This interaction may cause a deviation of the actual bubble sizes from the ones determined by the theoretical calculations. Nevertheless, the model allows the pumping modes to be approximated and is therefore helpful for an initial geometrical design of the tapered channel. Furthermore, the theoretical evaluation sheds light on and enables the investigation of the different influencing parameters, in particular the phenomenon of contact-line pinning,

responsible for the different pumping modes in tapered channel structures.

4.2 Pumping efficiency

For the investigation of the pump performance, the channels were supplied by the syringe pumps with a total gas flow varying from $\Phi_{gas} = 50$ to 620 µl min^{-1}. The single channel covers an active area of 1 cm^{-2}, thus, using Eq. 7 and replacing the mass flow rate by a volumetric flow rate with a density of $\rho_{CO_2} = 1.78$ kg m^{-3}, the gas flow rates corresponds to electric current densities between $i = 20$ to 240 mA cm^{-2}. These current densities cover the typical operation conditions of common DMFCs with operation temperatures up to 60°C, see for example the power spectrum in (Yang et al. 2005a, b; Ge and Liu 2005).

The pumping performance of the different channels is investigated on the basis of the pump efficiency p_{eff} defined as the ratio between the measured liquid flow rate to the applied gas flow rate. Measurements were performed for ten minutes and repeated four times for each gas flow at different days to account four a possible variation of surface properties. The average value of the flow rates and its standard deviation were used to determine the pump efficiency p_{eff}. In Fig. 6, p_{eff} for a single-tapered channel is plotted against the total gas flow rate for different tapering angles of $\alpha = 1.5°$ and 3°. The measured pump efficiencies are 2.5 to 13.2 times larger than required for the MOR ($p_{eff}^{MOR} = 1\%$). The 1.5° channel shows a 2.3 times larger pump efficiency (up to 13.2%) compared to the 3° channel (up to 3.8%). This higher efficiency is due to the blocking mode dominating in the 1.5° channel design whereas the non-blocking mode predominates in the 3° channel and allows for more liquid to bypass the moving bubbles.

In the non-blocking mode of the 3° channel, the liquid bypasses cause high bubble mobility and the bubbles move comparatively fast. Therefore, interactions between the bubbles generated at the different gas inlets play a minor role, e.g. only very few bubble merges were observed. Each bubble that moves through the channel transports a certain amount of liquid partially by drag and partially by displacement. A higher gas flow rate leads to an increase of
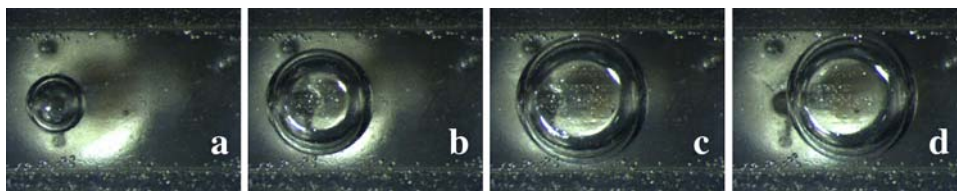
Fig. 5 Time sequence of a growing bubble above the centre inlet (inlet 2) of the tapered channel. **a** Initial bubble growth; **b** bubble touching the upper and lower channel wall; **c** deformed bubble shortly before bubble detachment; **d** detached bubble moving in the non-blocking mode towards the outlet
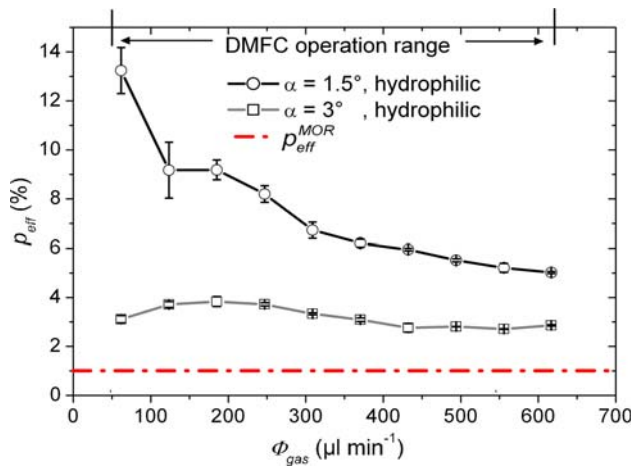
Fig. 6 Pump efficiency of a single-tapered channel plotted against the gas flow rate for different taper angles α

Fig. 7 Pump efficiency of a single-tapered channel with and without surface treatment plotted against the gas flow. The bottom channel surfaces are covered with a porous transport layer (PTL) to simulate configurations similar to DMFC operation

the bubble generation frequency, but the amount of liquid transported by each bubble does not change significantly. Thus, the liquid flow rates increase proportionally to the gas flow rates leading to a roughly constant p_{eff}. The 1.5° channel with the dominating blocking mode shows a completely different behavior. In the blocking mode, the liquid flow rates are dominated by the volume of the liquid fragments displaced or enclosed by moving bubbles that block the channel. The volume of these fragments is a result of a complex interaction between growing and moving bubbles generated at the three gas inlets. Presumably, corner flow in the channel edges also has a significant influence. For these reasons, the decrease of p_{eff} at increasing gas flow rates is difficult to interpret in detail but a possible explanation could be the following: The liquid flow rates increase at increasing gas flow rates. Thus, a higher actuation pressure is required to transport the fluids. The actuation pressure is proportional to the bubble length, so the bubbles grow larger as the gas flow rate increases. The increment in bubble size increases the overall gas load in the channels. As a consequence, the liquid fragments transported by the bubbles become smaller at higher gas flow rates. This results in a sub-proportional increase of the liquid flow rates which leads to a decrease of p_{eff}.

Subsequently, surface properties were modified to represent more realistic DMFC operation conditions. The channel bottom was covered by a porous transport layer (PTL) of 180 μm thickness (SGL, ®SIGRACET GDL31-BA). For the hydrophilic configuration, the PTL has also been made hydrophilic by plasma activation. The gas flow supplied through the inlets now has to flow through the PTL before it reaches the channel. This results in numerous small bubbles ejecting from the PTL. The bubbles merge and form larger bubbles. If a bubble reaches the size that exceeds the pinning threshold, the bubble moves towards
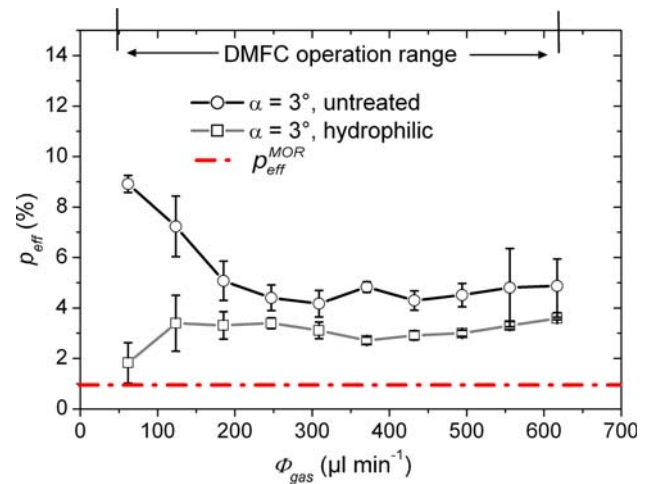
the increasing channel cross-section. The bubble configuration is much more irregular than in the configuration without the PTL and the results are difficult to interpret in detail. For example, we could not find a satisfactory explanation for the initial increase of p_{eff} at low gas flow rates in the hydrophilic case as depicted in Fig. 7. However, a few general conclusions can be drawn: It can be seen that in the hydrophilic configuration, the PTL does not significantly influence the pumping performance. The dominating mode is still the non-blocking mode. The results are very similar to those measured without the PTL plotted in Fig. 6. Due to the complete wetting at the PTL, the bubbles hardly touch the channel bottom and the triple-phase contact-line is very small. Thus, pinning plays a minor role.

In the untreated configuration, exclusively the blocking mode occurs. Similar to the 1.5° channel, p_{eff} first decreases with increasing gas flow. As the gas flow rate exceeds $\Phi_{gas} = 200$ μl min^{-1}, the moving bubbles start filling the complete channel. Each time such a bubble moves into the gas collection channel and flushes into the reservoir, roughly the same amount of liquid is transported in pump direction. As a consequence, p_{eff} remains roughly constant as the frequency of pumping bubbles increases with increasing gas flow rates.

Photographs of moving bubbles in the investigated configurations are depicted in Fig. 8. The photographs confirm the finding of the dominating non-blocking mode in the 3° channel (Fig. 8a) and the dominating blocking mode in the 1.5° channel (Fig. 8b). As mentioned above, in the hydrophilic configuration the coverage of the channel bottom with the PTL leads to smaller bubbles moving in the non-blocking mode (Fig. 8c). In contrast, as depicted in

Fig. 8 Top view of moving bubbles in tapered channels. **a** Non-blocking mode, hydrophilic, $\alpha = 3°$. **b** blocking mode, hydrophilic, $\alpha = 1.5°$. **c** non-blocking mode, hydrophilic, channel bottom covered with a porous transport layer (*PTL*), $\alpha = 3°$. **d** Blocking mode, untreated, channel bottom covered with a PTL, $\alpha = 3°$
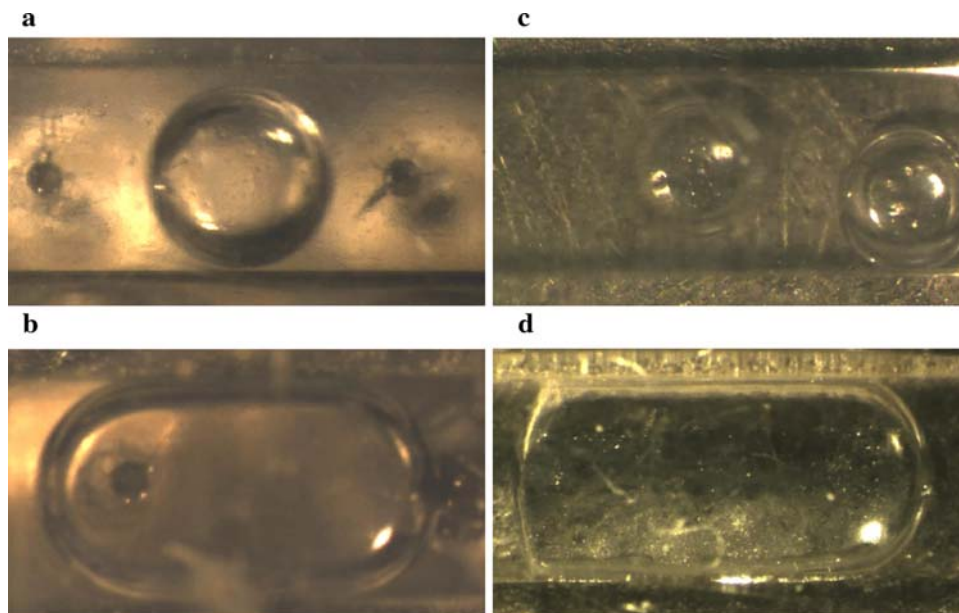

Bubble movement

Fig. 8d, an untreated PTL causes severe pinning. The back meniscus of the bubble is clearly flattened whereas the front meniscus is close to forming a hemisphere. The pump efficiency of this configuration is 1.8 times higher on average than in the hydrophilic configuration (as demonstrated in Fig. 7). Though hydrophilization increases the propelling capillary pressure differences over the single bubbles, here, it does not lead to higher pump rates. In fact, in the considered configuration, the higher capillary pressure causes the bubbles to move through the channels without blocking them which results in an even lower p_{eff}.

In summary, we found three different characteristic operation regimes of the capillary-driven bubble pump in single tapered channels. The first one is the non-blocking pumping mode (3° channel hydrophilic) in which p_{eff} remains roughly constant over the gas flow rates considered. The second one is the blocking mode with liquid fragments enclosed by the moving bubbles ($\alpha = 1.5°$ hydrophilic and $\alpha = 3°$ untreated with PTL $\Phi_{gas} < 200 \, \mu l \, min^{-1}$). In this case, p_{eff} decreases with increasing gas flow rates. The third one is the blocking mode with bubbles filling the complete channel ($\alpha = 3°$ untreated with PTL, $\Phi_{gas} \geq 200 \, \mu l \, min^{-1}$) for which p_{eff} remains again roughly constant over the various gas flow rates considered.

Figure 9 shows the pump efficiency in a double-tapered T-shaped channel as depicted in Fig. 1c(ii), again for two different configurations; a hydrophilic and an untreated channel surface. The channel bottom has been modified so that now 2×3 inlets are used to pump the gas into the side channels. In the hydrophilic case, the advancing contact
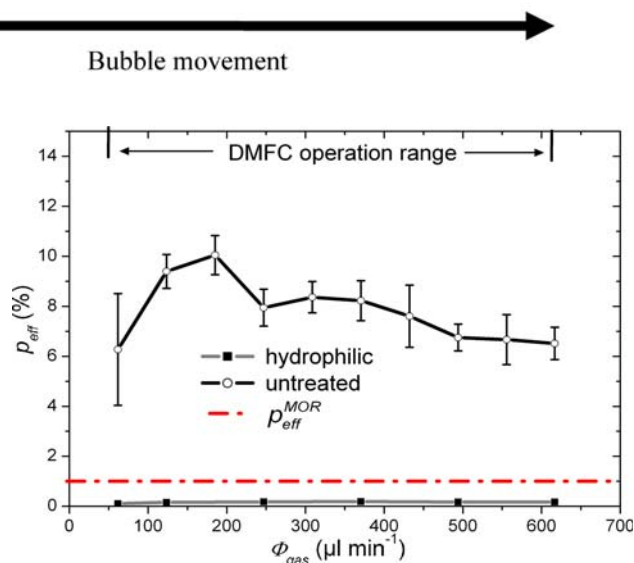
Fig. 9 Pump efficiency of a double-tapered T-shaped channel as shown in Fig. 3b plotted against the gas flow rate. In the untreated configuration, the channel is covered with a porous transport layer (PTL) to simulate more realistic DMFC operation conditions

angle is $\theta_{ad} = 5° \pm 3°$ and the receding one is $\theta_{rec} = 0°$, thus, the triple-phase contact line is very small. The opening angle of the side channel is 10°. Assuming again a contact angle hysteresis at the inlets of about 25°, the largest bubble calculated with Eqs. 1, 3 and 5 that could occur in the side channel would be about 0.5 mm long. The side channel, however, is 1.1 mm wide, so growing bubbles in the side channels move into the centre channel before they block the recirculation path for liquid displaced by moving bubbles in the centre channel. The major fraction of the liquid displaced by moving large bubbles in the

Fig. 10 Top view of anode flow fields with $\alpha = 3°$ during DMFC operation. **a** Three parallel single-tapered channels as depicted in Fig. 1c(i). **b** Three double-tapered T-shaped channel as depicted in Fig. 1c(ii)


Bubble movement
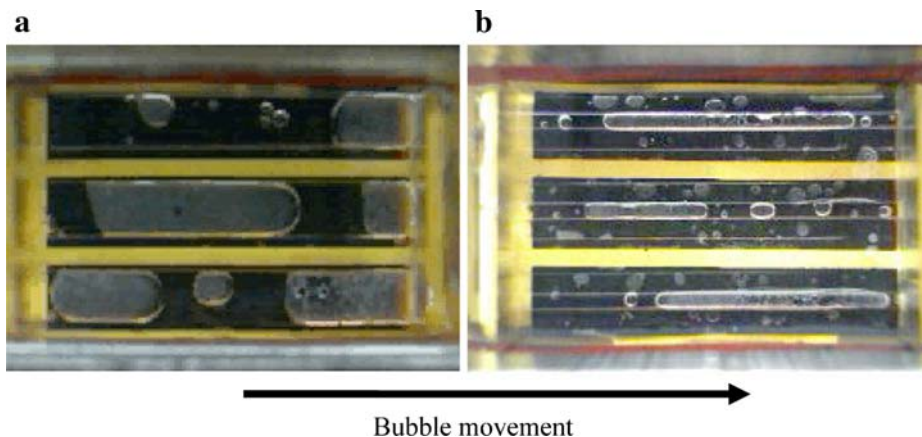
centre channels circulates directly around these bubbles and the pump efficiency almost vanishes.

The untreated channel shows pump efficiencies between 6 and 10%. Here, growing bubbles in the side channels pin and block the recirculation path. Thus, a significant amount is pumped. This configuration is applicable for the passive DMFC because it pumps six to ten times more methanol than the MOR would require.

4.3 The passive DMFC in operation

Finally, two configurations suitable for DMFC supply were tested in a fully passive DMFC, the untreated single-tapered channel and the untreated double-tapered T-shaped channel both with opening angles of $\alpha = 3°$.

Figure 10 shows a top view of the two different flow fields during DMFC operation. Internally generated CO_2 bubbles moving in the blocking mode supply the fuel cell with methanol. The channel bottom is covered by a PTL as in the experiments with the previously studied, untreated 3° channel. In Fig. 10a, the menisci of the back of the bubbles are clearly flattened indicating that contact-line pinning has a significant influence leading to the blocking pumping mode. The power performance of long-term experiments at a constant current density of $i = 20$ mA cm^{-2} is depicted in Fig. 11. The electric power output, as determined from the measured current and voltage, is displayed as a function of time. In the beginning of the discharging period, a comparatively rapid decline in power can be observed which is due to the formation and accumulation of water at the cathode that partially blocks the active area and thus reduces oxygen supply. The accumulated water forms droplets and after reaching a critical size, gravity causes water to drip off. Such behavior has also been observed, e.g. by Lai et al. (2008). The power fluctuations (e.g. Fig. 11 black line between 2 and 4 h of operation time), are caused by the formation and dripping of water at the cathode. Passive water transport and removal as discussed
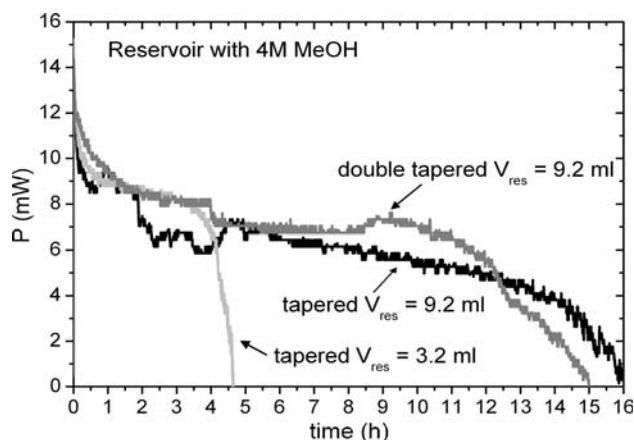
Fig. 11 Long-term performance of the fully passively operating DMFC for different reservoir fillings and for different channel types at ambient temperature ($T = 23°C$)

e.g. by Jewett et al. (2007) and Lai et al. (2008) is not addressed in this work but would probably improve and stabilize the performance of the considered passive DMFC. After the initial power decline, a period with a roughly constant power output follows. During this period, the methanol concentration in the reservoir decreases because of crossover and the MOR, but still enough methanol is transported to the active area of the anode and the power output is presumably limited by the passive oxygen supply at the cathode. At the end of the discharging period of each experiment, the major part of the methanol is consumed and the rapid decline of power is caused by undersupply of methanol. It can be seen from Fig. 11 that the runtime of the cell before it stops operation due to starving is proportional to the filling volume of the reservoir. A total filling volume of 3.2 ml (4 M MeOH) leads to power breakdown after about 4 h continuous operation, while a filling of 9.2 ml enables a continuous runtime of 15 h. This indicates that the cell operates until the methanol initially supplied to the reservoir has been completely consumed. The passive supply mechanism obviously operates properly

under the defined experimental conditions with a horizontal oriented DMFC. To ensure an orientation independent functionality of the proposed capillary-driven bubble pump, a downscaling of the geometry is required as indicated by the discussion on the influence of gravity in Sect. 2.4 which will be subject to future work.

The performance of the DMFC with the incorporated double-tapered T-shaped channel flow field is very similar to the performance with the single-tapered flow field. In Fig. 10b, the gas bubbles blocking the side channels of the T-shape are clearly visible, indicating that a sufficient pump efficiency can be achieved by the moving bubbles in the centre channel. In both cases, the fuel cells were operated passively at ambient temperature ($T = 23$°C) and pressure ($p = 1$ atm) with no external actuation or support of any kind.

5 Conclusions

A capillary-driven bubble pump for degassing and fuel supply has been developed and applied to realize a passive DMFC. Two pumping modes of moving gas bubbles were identified that lead to different capillary-induced liquid flow rates. These are the blocking and the non-blocking modes which have been shown to depend on geometry and wetting properties in the channels. The pumping modes were analyzed by a model and experiments. The key parameters identified for the pump performance are the opening angle α of the tapered channel and the contact angle θ and its hysteresis on the channel walls as well as the channel design (T-shaped or single-tapered). Hydrophilic channel walls ($\theta \approx 5$°) in the double-tapered T-shaped channel design resulted in degassing in the non-blocking mode with hardly any liquid flow induced by the moving bubbles ($p_{eff} < 0.5\%$), whereas the single tapered channel with hydrophilic walls and an opening angle of $\alpha = 1.5$° showed the highest pump efficiency of up to $p_{eff} = 13.2\%$ observed in experiments. This wide range from hardly any liquid transport to a significant amount pumped by moving bubbles makes the studied approach attractive, not only for fuelling DMFCs, but also for passive transport of liquid in any kind of micro-reactors with gaseous products or educts.

It has been shown by experiments that the operating DMFC with the incorporated passive supply mechanism does not require any external actuation or support for CO_2 bubble removal and fuel supply. The experiments performed, demonstrating continuous operation of up to 15 h, indicate that the runtime of such a passive DMFC is proportional to the amount of methanol initially supplied to the reservoir.

References

Ateya DA, Shah AA, Hua SZ (2004) An electrolytically actuated micropump. Rev Scient Inst 75:915–920

Becker H, Gärtner C (2000) Polymer microfabrication methods for microfluidic analytical applications. Electrophoresis 21:12–26

Chan YH, Zhao TS, Chen R, Xu C (2007) A small mono-polar direct methanol fuel cell stack with passive operation. J Power Sources 176:183–190

Chan YH, Zhao TS, Chen R, Xu C (2008) A self-regulated passive fuel-feed system for passive direct methanol fuel cells. J Power Sources 176:183–190

Cheng CM, Liu CH (2007) An electrolysis-bubble-actuated micropump based on the roughness gradient design of hydrophobic surface. J Microelec Sys 16:1095–1105

Dyer CK (2002) Fuel cells for portable applications. J Power Sources 106:31–34

Fei K, Chen WH, Hong CW (2008) Microfluidic analysis of CO_2 bubble dynamics using thermal lattice-Boltzmann method. Microfluid Nanofluid 5:119–129

Fries DM, von Rohr R (2008) Impact of inlet design on mass transfer in gas–liquid rectangular microchannels. Microfluid Nanofluid (online first)

Gao LC, McCarthy TJ (2006) Contact angle hysteresis explained. Langmuir 22:6234–6237

Ge JB, Liu HT (2005) Experimental studies of a direct methanol fuel cell. J Power Sources 142:56–69

Jewett G, Guo Z, Faghri A (2007) Water and air management system for a passive direct methanol fuel cell. J Power Sources 168:434–446

Jian R, Chu C (2004) Comparative Studies of Methanol Crossover and Cell Performance for a DMFC. J Electrochem Soc 151:69–76

Kho BK, Bae B, Scibioh MA, Lee J, Ha HY (2005) On the consequences of methanol crossover in passive air-breathing direct methanol fuel cells. J Power Sources 142:50–55

Lai QZ, Yin GP, Zhang J, Wang ZB, Cai KD, Liu P (2008) Influence of cathode oxygen transport on the discharging time of a passive DMFC. J Power Sources 175:458–463

Langbein D (2002) Capillary Surfaces; Shape-Stability-Dynamics, in Particular under Weightlessness. Springer, Berlin-Heidelberg

Litterst C, Eccarius S, Hebling C, Zengerle R, Koltay P (2006) Increasing µDMFC efficiency by passive CO_2 bubble removal and discontinuous operation. J Micromech Microeng 16:248–253

Litterst C, Metz T, Zengerle R, Koltay P (2008) Static and dynamic behaviour of gas bubbles in T-shaped non-clogging microchannels. Microfluid Nanofluid 5:775–784

Liu JG, Zhao TS, Chen R, Wong CW (2005) The effect of methanol concentration on the performance of a passive DMFC. Electrochem Com 7:288–294

Lu GQ, Wang CY (2004) Electrochemical and flow characterization of a direct methanol fuel cell. J Power Sources 134:33–40

Meng DD, Kim CJ (2008) Micropumping of liquid by directional growth and selective venting of gas bubbles. Lab Chip 8:958–968

Nguyen NT, Wereley ST (2002) Fundamentals and Applications of Microfluidics. Artech House Books, Boston

Park KW, Choi JH, Lee SA, Pak C, Chang H, Sung YE (2004) PtRuRhNi nanoparticle electrocatalyst for methanol electrooxidation in direct methanol fuel cell. J Catalysis 224:236–242

Paust N, Litterst C, Metz T, Zengerle R, Koltay P (2008) Fully passive degassing and fuel supply in direct methanol fuel cells. In: Proceedings of 21st IEEE MEMS, Tucson USA, pp 34–37

Wong CW, Zhao TS, Ye Q, Liu JG (2005) Transient capillary blocking in the flow field of a micro-DMFC and its effect on cell performance. J Electrochem Soc 152:1600–1605

Yang H, Zhao TS (2005) Effect of anode flow field design on the performance of liquid feed direct methanol fuel cells. Electrochem Acta 50:3243–3252

Yang H, Zhao TS, Ye Q (2005a) In situ visualization study of CO_2 gas bubble behavior in DMFC anode flow fields. J Power Sources 139:79–90

Yang H, Zhao TS, Ye Q (2005b) Pressure drop behavior in the anode flow field of liquid feed direct methanol fuel cells. J Power Sources 142:117–124